

Estimation of the Survivability of Boron Carbide and Steel Struck by the Direct FEL X-Ray Beam of LCLS

Alyssa A. Prinz

Mail Stop 20, SLAC National Accelerator Laboratory, Menlo Park, CA, 94025, USA

aaprinz@slac.stanford.edu

Abstract

A framework for estimating the energy deposited in a material struck by a direct FEL x-ray beam is presented. This framework is applied to the case of boron carbide and stainless steel struck by the FEL beam of the Linac Coherent Light Source (LCLS), and the results are compared to the thermal damage thresholds of these materials. The ability of these materials to withstand the beam is dependent on the photon energy, the distance between the material and the undulator, and the degree of beam focusing.

1. Introduction

In recognition of their potential to facilitate scientific research, free-electron lasers (FELs) are being constructed around the world. These facilities present a new challenge to radiation safety professionals: the need to insure proper containment of an x-ray beam that has sufficient energy density to vaporize solid materials. When the beam of a typical FEL, such as the Linac Coherent Light Source (LCLS), is focused to a spot size of a few microns, no known solid material can withstand it. Even when the beam is unfocused, it may still carry sufficient energy density to vaporize metals and possibly even ceramics.

If collimators or stoppers that protect personnel must be located in areas where an FEL beam can be focused, then air (for soft x-rays) or water (for hard x-rays) is a suitable absorbing material. (See Appendix A for example designs of an air-based collimator and water-based beam stop.) Solid materials can be considered in areas where the beam is unfocused or partially focused, provided that the chosen material is shown to be capable of withstanding the maximum energy density of the beam indefinitely.

We have developed a framework for estimating the energy density that an FEL can deliver to a material. We present this framework and apply it to the case of LCLS for two materials of interest: 304 stainless steel (the material of LCLS's vacuum chambers) and boron carbide (a low-Z ceramic with a high melting point, used in LCLS's photon stoppers and collimators). Comparing the estimates to the measured damage thresholds of these materials (both melt threshold and multi-pulse "thermal fatigue" threshold), we determine where along the LCLS beam line these materials can be relied upon to stop the FEL beam, and where they are likely to fail.

Though potentially relevant to the long-term chemical and mechanical stability of materials, radiation damage (*e.g.*, accumulation of lattice dislocations) has not been included in this analysis.

2. Parameters of the LCLS FEL Beam

The x-ray energy in the LCLS FEL beam is tunable from 0.25 keV to roughly 12 keV. The beam is pulsed, with a pulse rate of 120 Hz. The total energy of each pulse is a few millijoules. The total power in the beam is fairly small (a Watt or less), but this power is spread over a small area (the beam spot size varies from a few millimeters when unfocused to a few microns when focused). In addition, the pulse duration is very small, with a minimum of about 10 femtoseconds. This is much shorter than the time scale for heat flow in materials. The material will therefore respond as though the energy of the pulse were delivered instantaneously. Further details of the FEL beam parameters are given in Section 7.1.

3. General Approach to the Energy-Density Calculation

We take as input the estimates of pulse energy, spot size and angular divergence (as functions of photon energy) of the FEL beam leaving the undulator, as provided to us by LCLS accelerator physicists. (These estimates are based on simulations of FEL generation within the undulator.) We then calculate, using the methodology of Gaussian beam optics, the beam spot size at locations of interest (*e.g.*, stoppers). From pulse energy, spot size, and properties of the absorbing material (specifically the mass-energy absorption coefficient and density), we calculate the energy “dose” that each pulse delivers in units of eV/atom. The results are then compared to experimentally measured damage thresholds. Each of these steps will be described more fully in the sections that follow.

4. Spot Size Evolution: An Application of Gaussian Beam Optics

In this section we present a brief introduction to Gaussian beam optics, highlighting the equations relevant for calculating the beam spot size downstream of the undulator.

Beams of transversely coherent electromagnetic radiation, of which optical lasers and FELs are examples, have certain characteristics in common. One is that their intensity distribution along a plane perpendicular to the beam can be described as a linear superposition of certain modes, such as the ones shown in Figure 1.

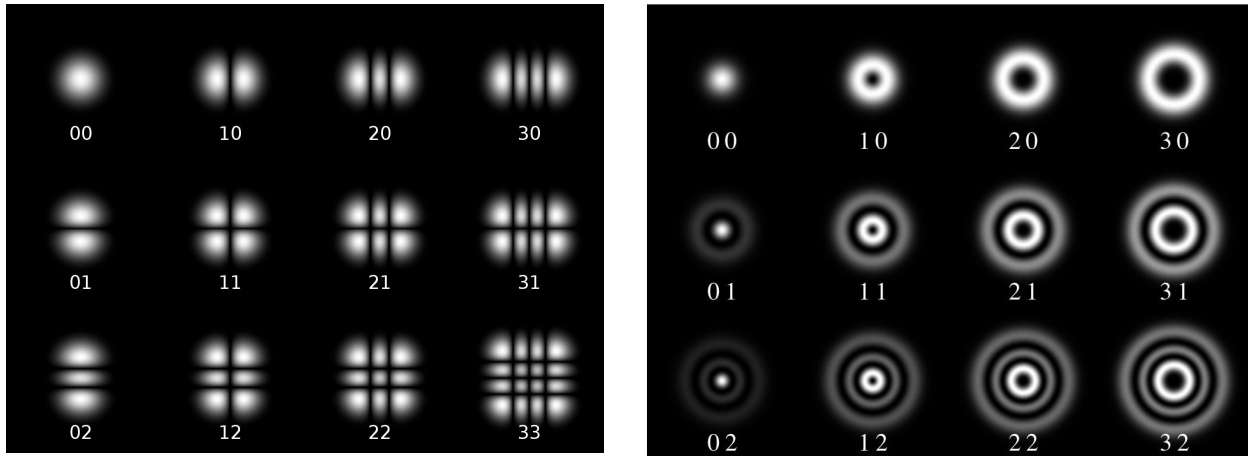


Figure 1. Various laser modes. On the left: Hermite-Gaussian modes, typical of lasers with rectangular resonance cavities. On the right: Laguerre-Gaussian modes, typical of lasers with cylindrical resonance cavities. The left and right images are reprinted from DrBob [1] and Ziofil [2], respectively.

The simplest of all possible modes is the TEM00 mode (labeled “00” in the figure). It is reasonable to assume that an FEL being used as a light source will be tuned to minimize all modes other than TEM00, since TEM00 produces the smallest, most uniform beam spot.

Another view of the intensity distribution of the TEM00 mode is shown in Figure 2. It is a two-dimensional Gaussian with peak on the beam axis. TEM00 beams are often referred to simply as “Gaussian beams.” A well-established formalism exists for describing the evolution of Gaussian beams as they travel and interact with optical elements. (See, for example, [3-6].)

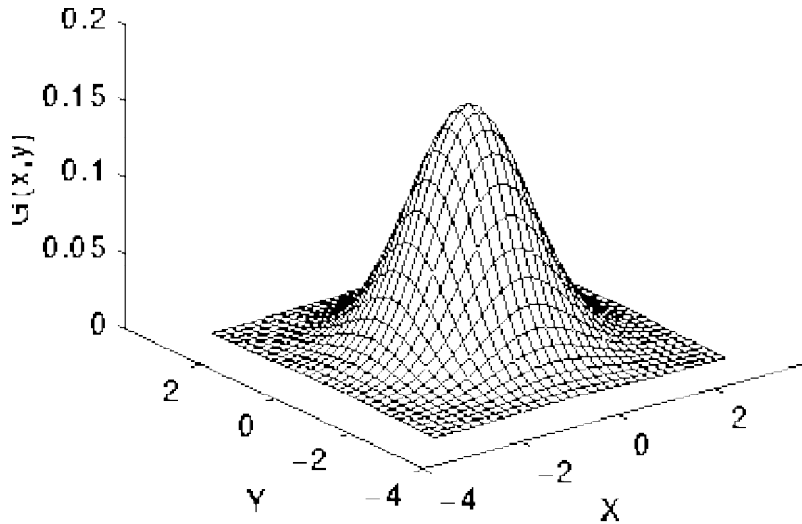


Figure 2. An example of the transverse intensity distribution of a TEM00 beam, otherwise known as a Gaussian beam.

In the absence of optical elements, a Gaussian beam will go through a point of minimum width, known as the beam waist. (This is located somewhere inside the undulator, in the case of an FEL.) Downstream of the waist the beam will expand indefinitely. This is illustrated in Figure 3, where the beam width as a function of travel distance is shown in blue. Overlaid in red is the beam intensity profile at the waist and at a location downstream. Note how the profile becomes shorter and wider as the beam travels.

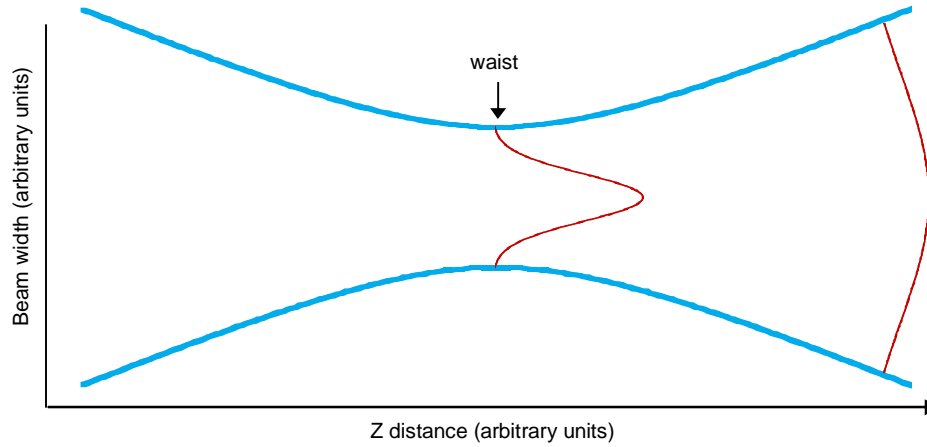


Figure 3. Change in width of a Gaussian beam as a function of propagation distance. The width is indicated in blue, and the transverse intensity profile at the waist and at a second location downstream is shown in red.

A few definitions are necessary at this point. The transverse intensity distribution of a Gaussian beam is described by the following equation

$$I(r) = \frac{2P}{\pi\omega^2} \exp\left[-\frac{2r^2}{\omega^2}\right] \quad (1)$$

where P is the pulse power (= total energy of the pulse / time duration of the pulse), r is the distance from the beam axis, and ω is the “ $1/e^2$ radius,” *i.e.*, the distance (from the beam axis) at which the intensity has dropped to $1/e^2$ of its maximum value. ω is one of various possible quantities one can use to specify the width of the beam. Other quantities in common use are σ (the standard deviation, or “RMS,” of the

Gaussian) and the full-width-at-half-maximum (FWHM). These three quantities can be inter-converted via the following equations:

$$\sigma = \omega/2 \quad (2)$$

$$\text{FWHM} = \omega\sqrt{2\ln(2)} \quad (3)$$

At the beam waist, the $1/e^2$ radius ω is known as ω_0 . The distance over which ω increases from ω_0 to $\sqrt{2}\omega_0$ is known as the Rayleigh length, L_R . As the distance (Z) increases, the curve of radius versus Z asymptotically approaches a straight line. The angle θ of this line relative to the Z axis is known as the far-field divergence. Figure 4 illustrates the quantities ω , ω_0 , L_R and θ .

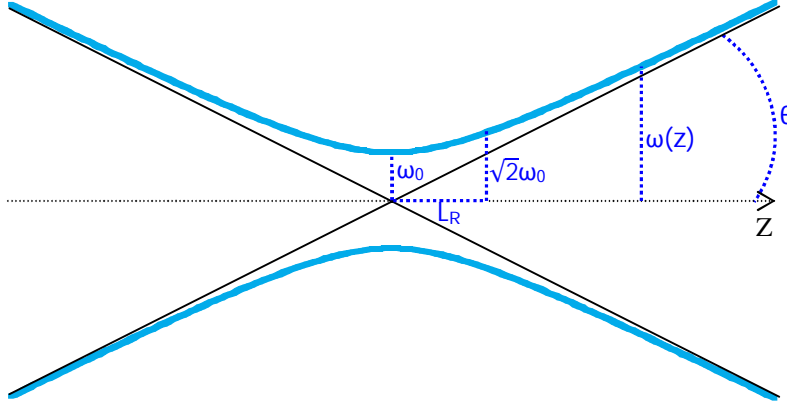


Figure 4. Gaussian beam width as a function of Z (light blue curve), showing asymptotically linear behavior and definitions of ω_0 , L_R and θ .

L_R , ω_0 and θ are all related, such that if one of them is known, the other two are known as well. They can be inter-converted via the following equations:

$$L_R = \pi\omega_0^2/\lambda \quad (4)$$

$$\theta = \lambda/(\pi\omega_0) \quad (5)$$

where λ is the wavelength of the FEL photons. Note that ω_0 and θ are inversely proportional: the smaller the waist, the faster the beam spreads as it travels.

Now that the relevant quantities have been defined, we can proceed to the useful results of Gaussian beam optics.

In the absence of optical elements, the evolution of the width of a Gaussian beam is described by the following equation:

$$\omega(Z) = \omega_0 \sqrt{\left(\frac{Z - Z_0}{L_R}\right)^2 + 1} \quad (6)$$

where Z is the location of interest and Z_0 is the location of the beam waist. Note that this equation is symmetric about the waist.

If the beam encounters a focusing optic (such as a stack of beryllium lenses or a K-B mirror system), it will converge to a new waist (the focal spot), after which it will once again expand. The value of ω_0 at

the new waist (ω'_0) is determined by the focal length f of the optic, along with the distance s from the original waist to the optic, as described by the following equation [3]

$$\omega'_0 = \omega_0 \left[\left(1 - \frac{s}{f}\right)^2 + \left(\frac{L_R}{f}\right)^2 \right]^{-\frac{1}{2}} \quad (7)$$

The location of the new waist can be found from the following equation [3]

$$\frac{s'}{f} = 1 + \frac{(s/f) - 1}{[(s/f) - 1]^2 + [L_R/f]^2} \quad (8)$$

where s' is the distance from the optic to the new waist. This reduces to the familiar thin-lens equation from geometric optics ($1/s + 1/s' = 1/f$) when $L_R/f \ll 1$.

Downstream of the optic, the beam evolution is once again described by Equation 6, but with values of Z_0 , ω_0 and L_R corresponding to the new waist. By repeated application of Equations 6 – 8, one can trace the beam evolution through a series of optical elements.

A few things should be noted at this point. One is the range of validity of the equations from Gaussian beam optics. They hold as long as the focusing is not too strong, specifically, as long as $\omega_0 \gg 2\lambda/\pi$. Also, apertures that clip more than an insignificant portion of the Gaussian's tails will render the beam non-Gaussian due to diffraction effects. A more complex formalism is then needed to describe the beam (see, for example, [7, 8]). An example of the impact of an aperture on a focused Gaussian beam is shown in Figure 5.

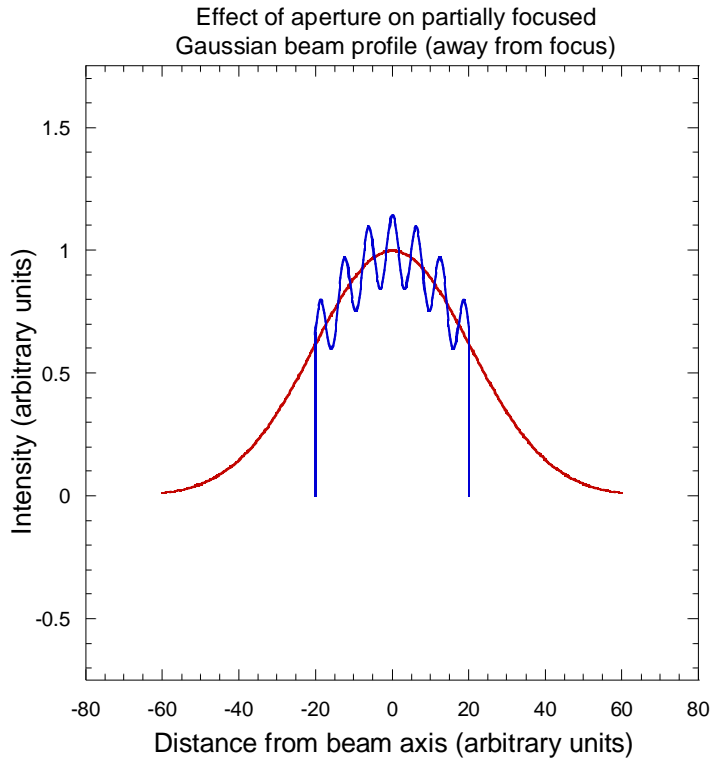


Figure 5. Example of the effect of an aperture on a focused Gaussian beam. The un-apertured beam profile is shown in red. The apertured profile, at a point partway between the aperture and the focal spot, is shown in blue.

Another thing to note is that beam widths calculated using the above methodology represent theoretical minimum values (often referred to as the “diffraction-limited spot size”). In practice, imperfections in beam quality and in optical elements always result in larger-than-theoretical beam widths.

Also of interest is the fact that a Gaussian beam can evolve independently in X and Y. For example, a beam that encounters a single focusing mirror (focusing in the X dimension, say) will converge in X while continuing to diverge in Y, resulting in an elliptical beam spot. The above set of equations are equally valid when applied to ω_x and ω_y separately.

A schematic of a typical geometry encountered at LCLS is shown in Figure 6. The shielding in the diagram could represent a vacuum chamber wall, hutch wall or beam stop. The smaller size of the focal spot relative to the original waist is a common situation, given that users often request the smallest possible spot size.

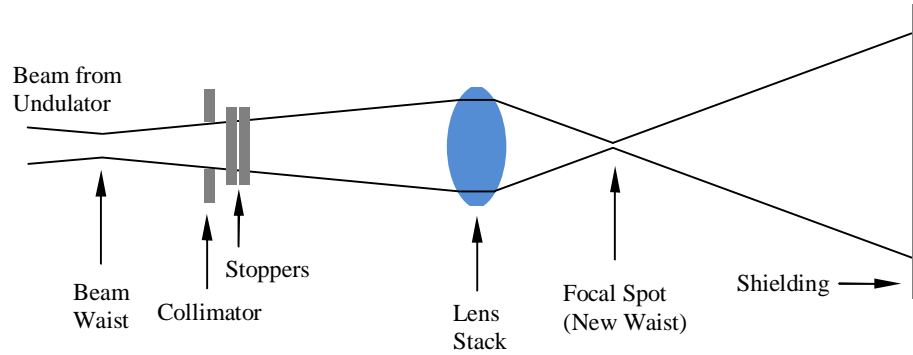


Figure 6. Schematic of typical x-ray beam geometry at LCLS.

5. Energy Deposition in Materials

The greatest energy deposition occurs on the beam axis, at the surface struck by the beam. We conservatively assume that the beam strikes the material at normal incidence. From Equation 1, the intensity (power per unit area) on the beam axis is $2P/(\pi\omega^2)$. At LCLS the pulses are short (tens of femtoseconds) and the time between pulses is long (milliseconds) compared to the time scale of heat flow in materials, so power is less relevant than energy deposited per pulse. Replacing P with G , where G is the total energy of the pulse, gives $2G/(\pi\omega^2)$ for the energy per unit area per pulse on the beam axis. The energy per unit volume per pulse (U) deposited at the material surface is given by

$$U = \frac{2GT}{\pi\omega^2} \frac{\mu_{en}}{\rho} \rho \quad (9)$$

where μ_{en}/ρ is the mass-energy absorption coefficient of the material, ρ is the density of the material, and a factor T has been added to account for imperfect beam transmission between the undulator and the point of interest (things such as mirror reflectivity and filter transmission would be included in T).

This could alternatively be expressed as the energy per atom per pulse (W) deposited at the surface

$$W = \frac{2GT}{\pi\omega^2 N} \frac{\mu_{en}}{\rho} \rho \quad (10)$$

where N is the atom number density of the material. Note that for elliptical beam spots, ω^2 can be replaced by $\omega_x\omega_y$.

6. Measured Damage Thresholds

Measurements have been conducted of the damage induced in stainless steel and boron carbide by the focused FEL beam at LCLS [9, 10]. For boron carbide, a threshold for single-pulse damage was established which is consistent with melting as the damage mechanism. Thresholds for multi-pulse damage (*e.g.*, thermal fatigue) were investigated but not conclusively established. However, the tests established an energy deposition level that could be withstood for more than 10^5 pulses by each material. The results are as follows:

The onset of single-pulse damage in boron carbide occurred at 0.49 ± 0.08 eV/atom [10]. Boron carbide withstood 6.40×10^5 pulses of 0.16 eV/atom without any observable damage [10].

Stainless steel withstood 2.16×10^5 pulses of 0.28 eV/atom without any observable damage [9].

The single-pulse damage threshold of steel was not determined in the measurements. Instead we use the calculated melt threshold, 0.45 eV/atom, obtained by integrating the heat capacity of iron [11] from room temperature to 1400 °C (the lower end of the melting temperature range for 304 stainless steel [12]), conservatively omitting the heat of fusion.

7. Estimated Energy Deposition at LCLS

Equations 6 – 8 and 10 were used to estimate the energy deposition in 304 stainless steel and boron carbide as a function of distance from the undulator (Z) for unfocused FEL over the length of the LCLS experimental floor.

7.1 Inputs to the Calculation

The beam parameters used as inputs to the calculation consisted of the waist size (ω_0) and waist position (Z_0) inside the undulator, and the pulse energy (G). G and ω_0 were provided to us as functions of photon energy by the LCLS accelerator physicists [13]. In keeping with the United States regulatory requirement that accidental as well as normal operating conditions be considered, we based our calculation on the maximum pulse energy and minimum beam divergence that LCLS could credibly produce. The former is shown in Figure 7. The values of ω_0 corresponding to the minimum credible divergence are shown in Figure 8. We conservatively assumed that the waist was positioned as far downstream as possible, namely at the downstream end of the undulator.

For boron carbide we assumed a chemical formula of $B_{13}C_2$ [14], a density of 2.55 g/cm^3 , and an atom number density of $1.40 \times 10^{23} \text{ atoms/cm}^3$. Values of μ_{en}/ρ were obtained from CXRO [15] for photon energies below 1 keV, and from NIST [16] for higher energies. The results are shown in Figure 9.

For 304 stainless steel we assumed a density of 8.03 g/cm^3 and an atom number density of $8.8 \times 10^{22} \text{ atoms/cm}^3$. We considered two possible compositions: the one having the highest concentrations of non-Fe components allowed by the standard, and the one having the lowest concentrations. Values of μ_{en}/ρ were obtained from CXRO for energies below 1 keV and from NIST for energies above. At each energy, the maximum value of μ_{en}/ρ of the two compositions was taken. The result is shown in Figure 9.

The transmission (T) through the LCLS optics between the undulator and the experimental floor is shown in Figure 10. These optics consist of x-ray mirrors that do not focus the beam.

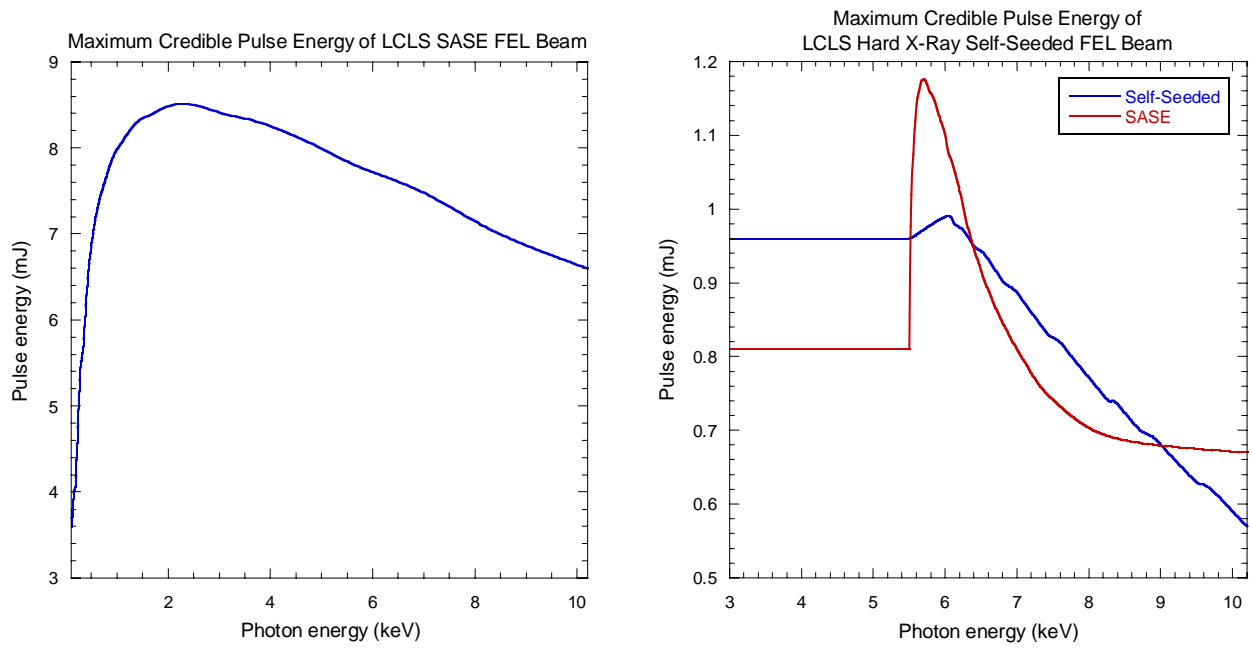


Figure 7. Maximum credible pulse energy of LCLS FEL. Left plot: Undulator running in SASE mode. Right plot: Undulator running in hard x-ray self-seeded mode. (In self-seeded mode, half of the undulator produces SASE beam while the other half produces self-seeded beam. The total pulse energy is the sum of the two.) In the right plot, no data were available between 3 and 5.5 keV. A flat extrapolation was applied.

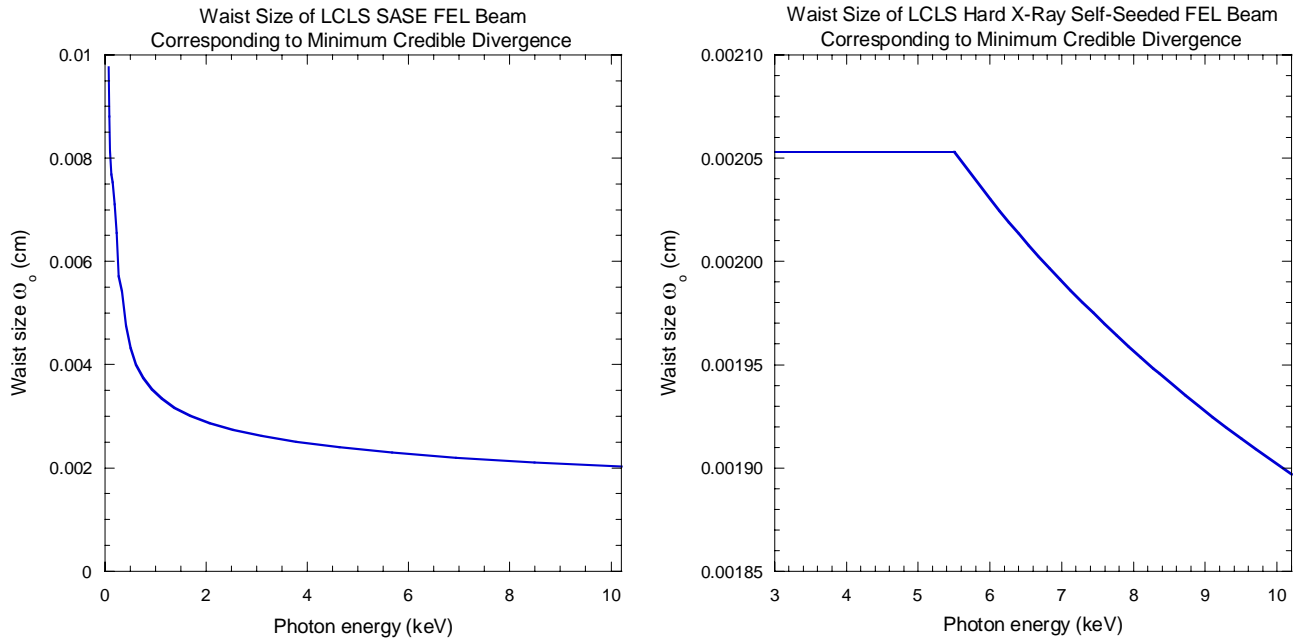


Figure 8. Waist size corresponding to minimum credible divergence of LCLS FEL. Left plot: Undulator running in SASE mode. Right plot: Undulator running in hard x-ray self-seeded mode. In the right plot, no data were available between 3 and 5.5 keV. A flat extrapolation was applied.

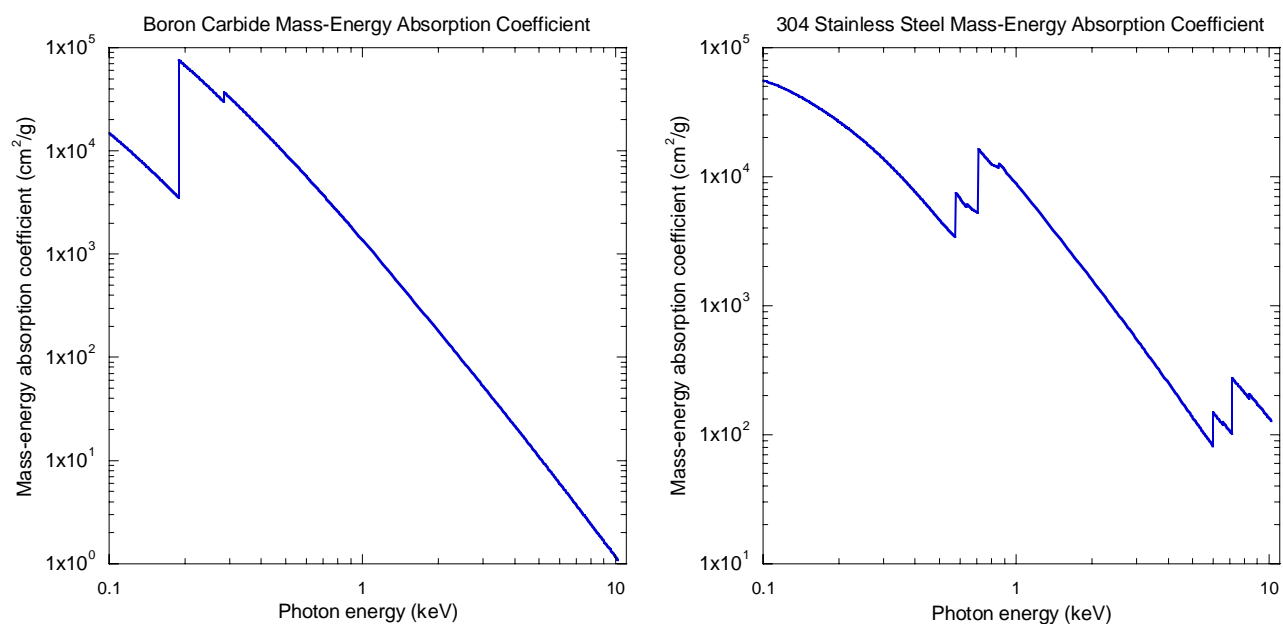


Figure 9. Mass-energy absorption coefficient (μ_{en}/ρ) for boron carbide (left plot) and for 304 stainless steel (right plot).

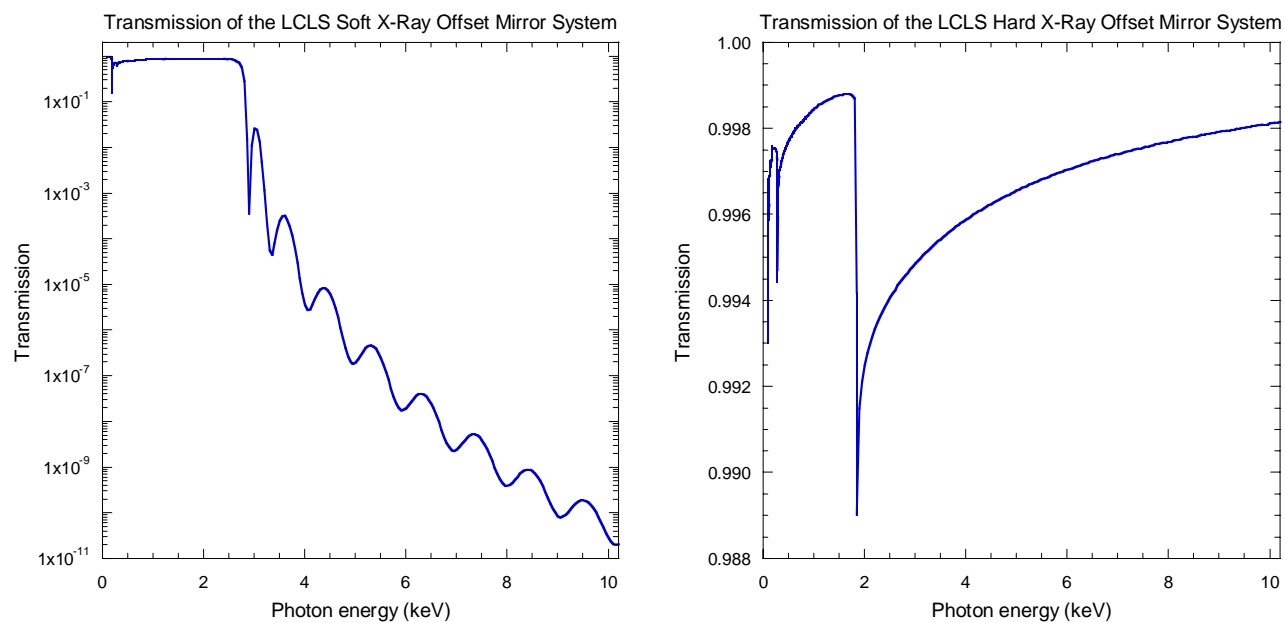


Figure 10. Transmission of the LCLS optics between the undulator and the experimental floor. Left plot: the optics system for soft x-rays. Right plot: the optics system for hard x-rays. The vertical axis is logarithmic in the left plot and linear in the right plot.

7.2 Calculation Results and Discussion

Figures 11 - 15 show the calculated energy deposition in boron carbide and steel from a normal-incidence strike by the unfocused LCLS FEL beam. They are two-dimensional plots of the energy “dose” W (in eV per atom per pulse) as a function of photon energy and distance from the undulator (Z). Figures 16 and 17 give an example of energy deposition by a partially-focused beam.

In each of these figures, the region below the horizontal line labeled “start of experimental floor” is the optical enclosure, containing collimators, mirrors and diagnostics. There are no focusing optics in the optical enclosure. In Figures 11-15, the experimental floor spans the region from the horizontal line to the top of the plot. In Figures 16 and 17, only a portion of the experimental floor is included (specifically, that spanned by the beam line in which the focusing occurs).

The term “MCB” in the figure titles stands for “Maximum Credible Beam,” and indicates that the calculations were performed for the maximum pulse energy and minimum beam divergence that LCLS could credibly produce. The outermost contour (*e.g.*, the 0.16 eV/atom contour in Figure 11) in every plot except for Figure 14 is the dose that the material can withstand for more than 10^5 pulses without damage, as specified in Section 6. (In Figure 14, the maximum dose is below this value.) We refer to this value as the material’s “safe threshold.” Note that the color scale is not consistent between the various plots.

Figure 11 indicates that energy deposition from unfocused LCLS SASE FEL can exceed the safe threshold of boron carbide in the optical enclosure, and also on the experimental floor for low photon energies.

Figure 12 shows the impact of an administrative control that limits the pulse energy to 1.5 mJ for photon energies below 0.5 keV: for components on the experimental floor, the energy deposition in boron carbide remains below the safe threshold at all photon energies.

Figure 13 indicates that the energy deposition in steel from unfocused LCLS SASE FEL is above the safe threshold over much of the experimental floor for nearly all photon energies. In the optical enclosure, the energy deposition is above the calculated single-pulse damage threshold (0.45 eV/atom) for most photon energies.

Figures 14 and 15 show the energy deposition in boron carbide and steel, respectively, from unfocused LCLS hard x-ray self-seeded beam. For boron carbide, the energy deposition is below the safe threshold at all locations. For steel, the safe threshold can be exceeded in the optical enclosure but not on the experimental floor. (The values at the lowest photon energies are unrealistically high due to our flat extrapolation of pulse energy and waist size below 5.5 keV.)

Figures 16 and 17 show energy deposition in boron carbide and steel, respectively, for SASE FEL that has been vertically but not horizontally focused by a curved mirror in LCLS’s SXR (“Soft X-Ray”) beam line. Near the focus, the dose to these materials can exceed both the safe threshold and the single-pulse damage threshold by more than two orders of magnitude. A worse situation (not shown in the figures) occurs when the beam is focused both vertically and horizontally, as is typical near the location of the experimental sample. There is a stopper (“Stopper S2B”) located fairly close to the focus. This stopper will need to be retrofitted to incorporate air before it can be relied upon for personnel protection purposes.

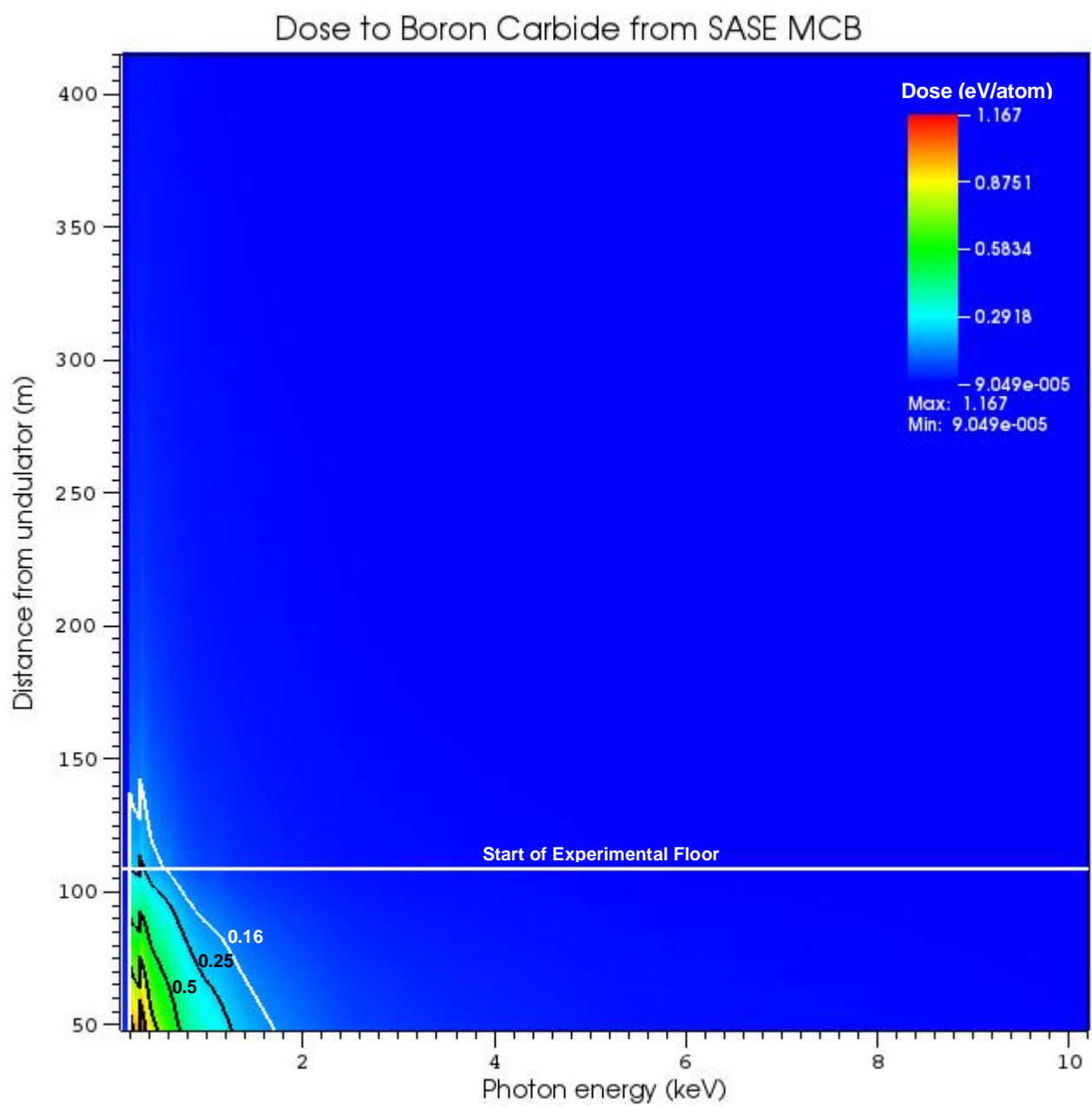


Figure 11. Calculated energy deposition in boron carbide from unfocused LCLS SASE FEL.

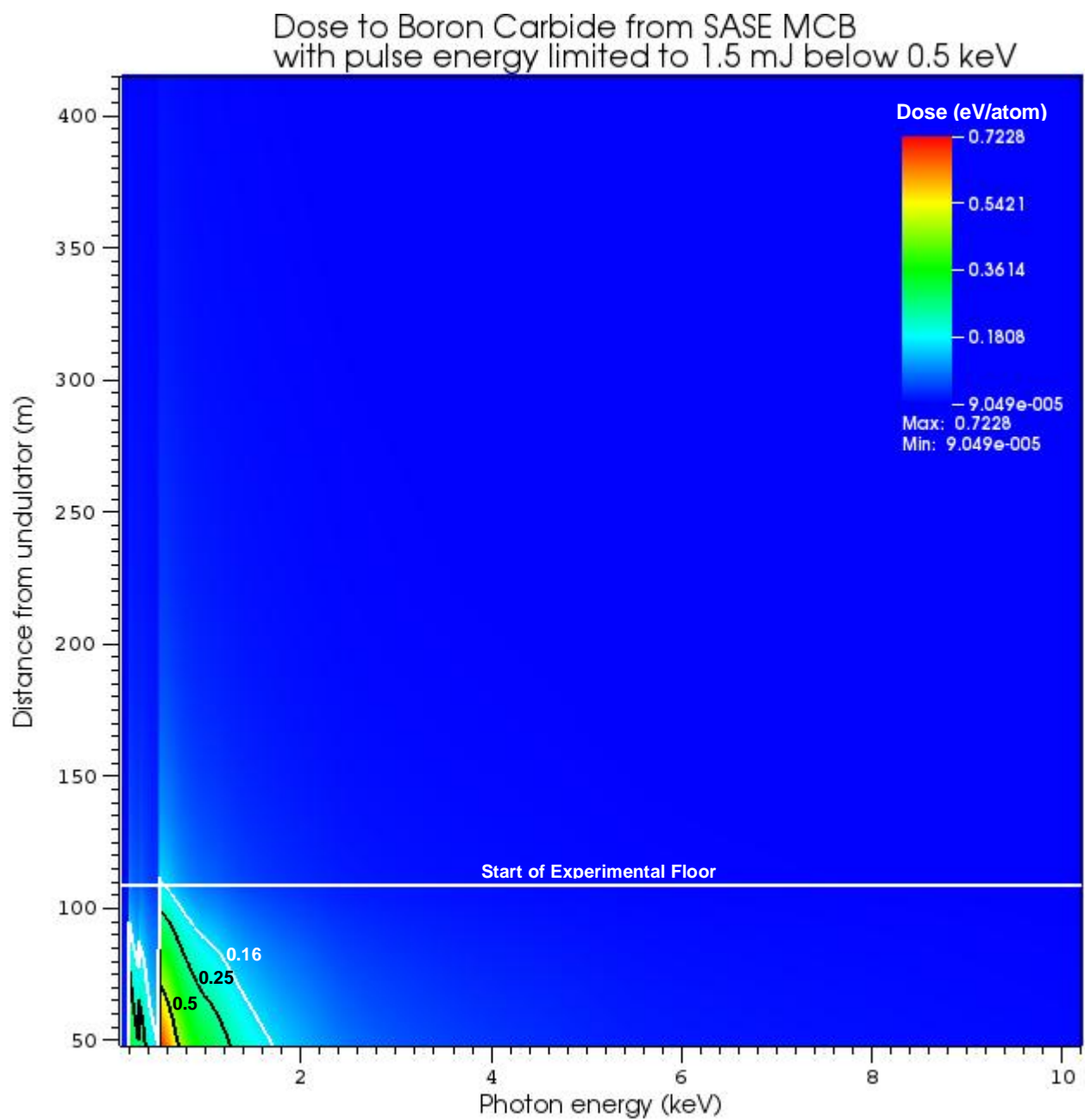


Figure 12. Calculated energy deposition in boron carbide from unfocused LCLS SASE FEL, under the assumption that the pulse energy is limited to 1.5 mJ for all photon energies below 0.5 keV.

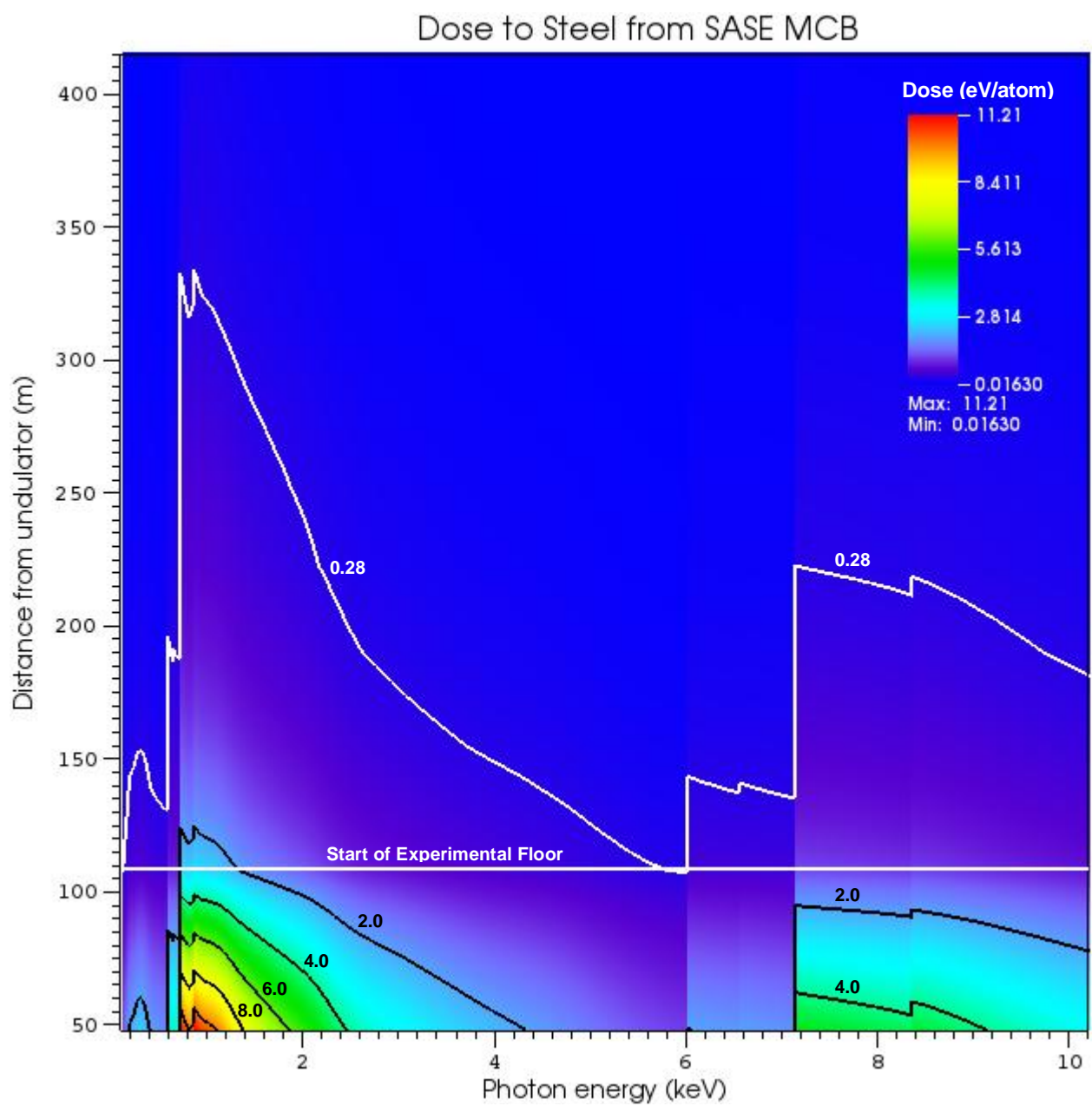


Figure 13. Calculated energy deposition in 304 stainless steel from unfocused LCLS SASE FEL.

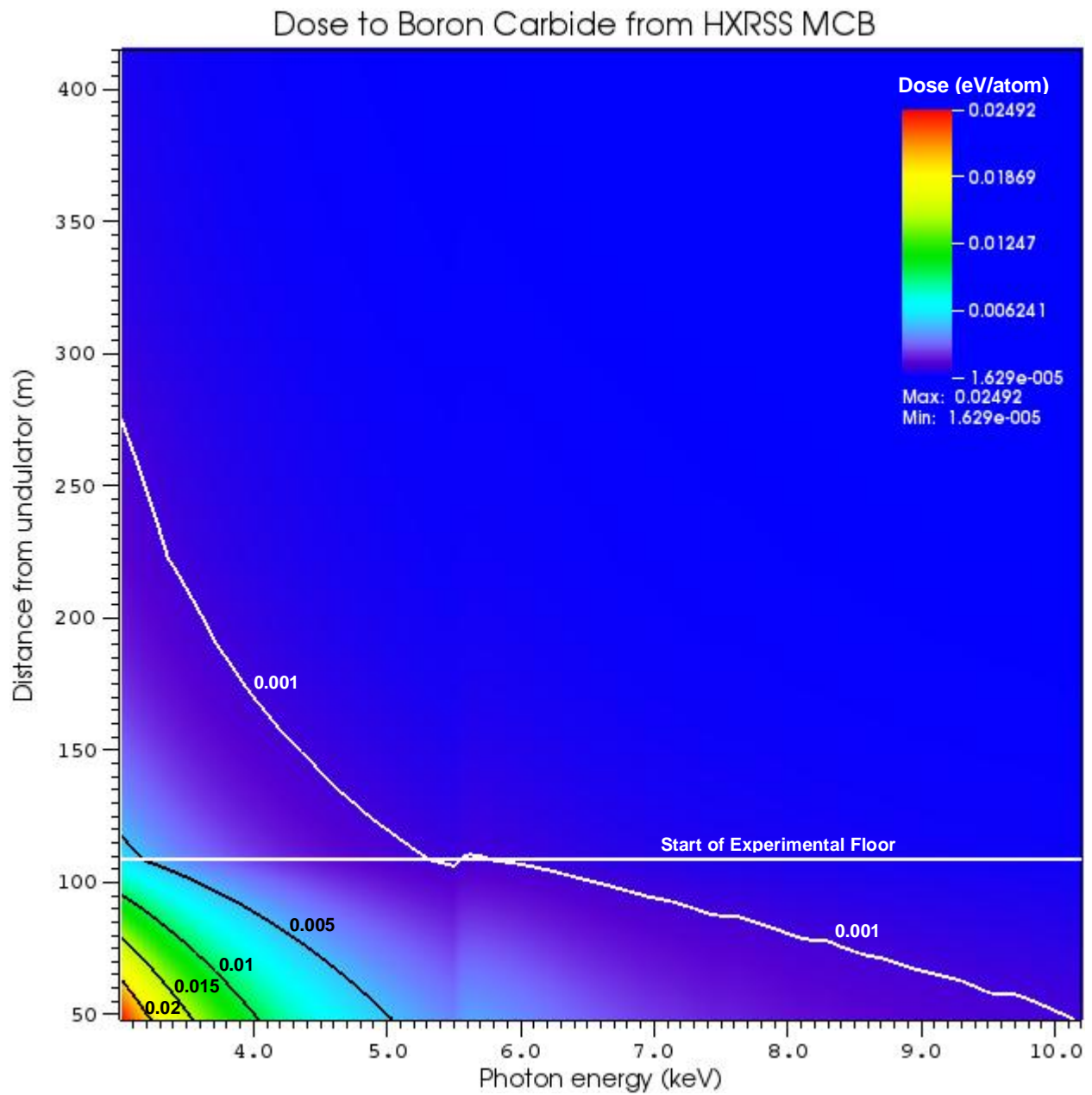


Figure 14. Energy deposition in boron carbide from unfocused LCLS hard x-ray self-seeded beam. The SASE that is produced concurrently with the self-seeded beam is included in the estimate.

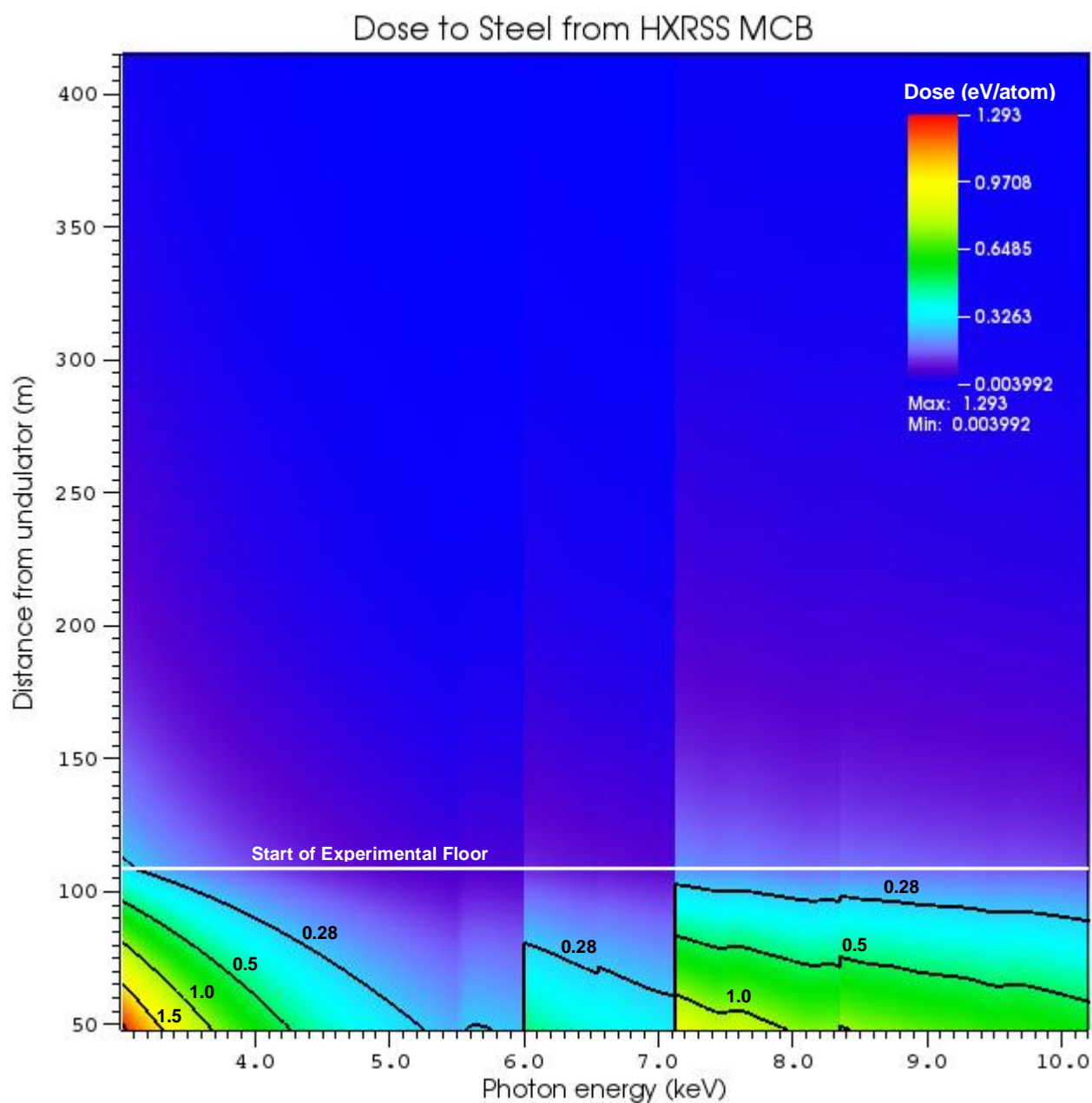


Figure 15. Energy deposition in 304 stainless steel from unfocused LCLS hard x-ray self-seeded beam. The SASE that is produced concurrently with the self-seeded beam is included in the estimate.

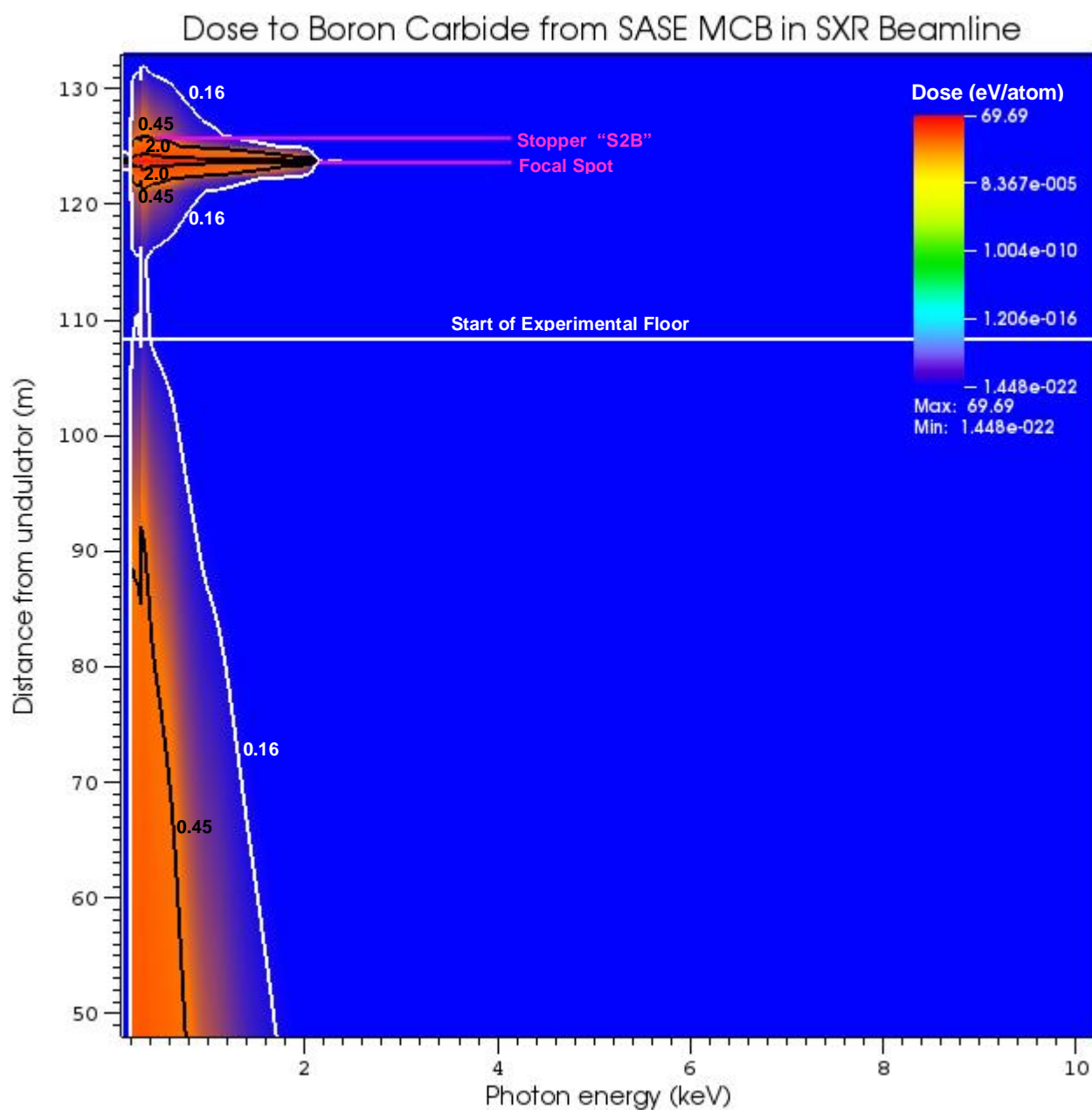


Figure 16. Calculated energy deposition in boron carbide from LCLS SASE FEL that has been vertically but not horizontally focused by the monochromator of the SXR beam line.

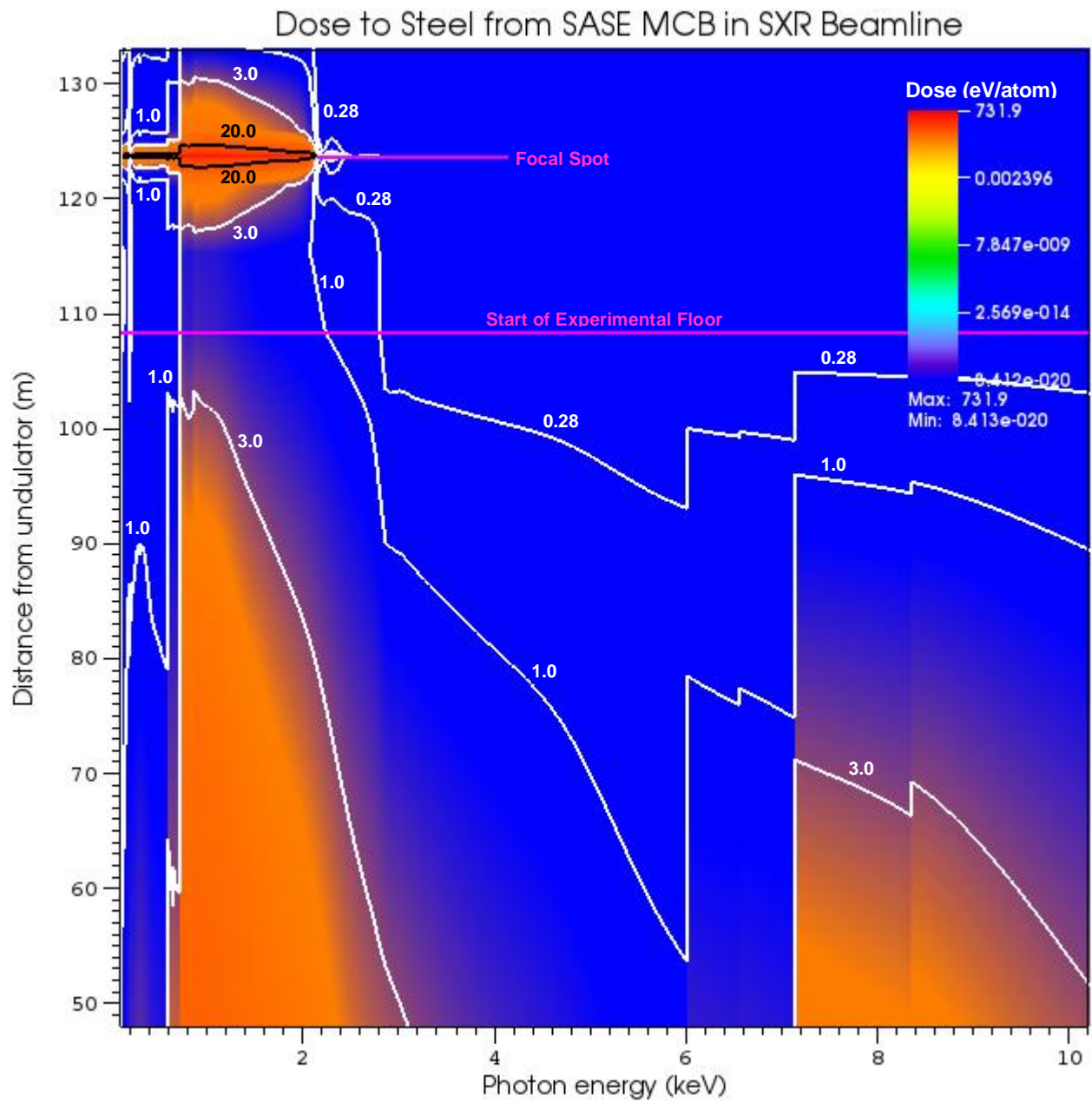


Figure 17. Calculated energy deposition in 304 stainless steel from LCLS SASE FEL that has been vertically but not horizontally focused by the monochromator of the SXR beam line.

References

1. Wikimedia Commons file "Hermite-Gaussian.png," <http://commons.wikimedia.org/wiki/File:Hermite-gaussian.png>, ©DrBob at <http://en.wikipedia.org>
2. Wikimedia Commons file "LG-wiki.jpg," <http://commons.wikimedia.org/wiki/File:LG-wiki.jpg>, ©Ziofil at <http://en.wikipedia.org>
3. S.A. Self, "Focusing of spherical Gaussian beams," *Applied Optics* **22**, Issue 5, page 658, March 1983.
4. "Gaussian beam," article on Wikipedia: http://en.wikipedia.org/wiki/Gaussian_beam, accessed July 2, 2013.
5. "Gaussian Beam Optics," Technical Guide published by CVI Melles Griot, <https://www.cvimellesgriot.com/Products/Documents/TechnicalGuide/Gaussian-Beam-Optics.pdf>
6. C.C. Davis, "Lasers and Electro-Optics: Fundamentals and Engineering," Cambridge University Press, New York, 1996.
7. G.D. Gillen, C.M. Seck and S. Guha, "Analytical beam propagation model for clipped focused-Gaussian beams using vector diffraction theory," *Optics Express* **18**, Issue 5, page 4023, March 2010.
8. "LightPipes: beam propagation toolbox for Matlab and Mathcad," software package for simulating diffraction and interference of light, published by Flexible Optical BV (a.k.a. OKO Tech), <http://www.okotech.com/lightpipes>
9. D. Fritz, M. Cammarata and S. Moeller, "Steel test results using focused FEL beam at the XPP instrument at 9keV," LCLS Memorandum to the SLAC RSO, November 1, 2011.
10. S. Moeller and J. Krzywinski, "Results of B4C survivability test at 2.7GeV (330eV) in the focussed beam of the SXR beamline," LCLS Memorandum to Sayed Rokni (SLAC RSO), August 6, 2013.
11. NIST (U.S. National Institute of Standards and Technology) Chemistry WebBook, NIST Standard Reference Database Number 69, <http://webbook.nist.gov/chemistry>
12. "AISI Type 304 Stainless Steel," Material Data Sheet published by ASM (Aerospace Specification Metals Inc.), <http://asm.matweb.com/search/SpecificMaterial.asp?bassnum=MQ304A>
13. H.D. Nuhn, "Maximum Credible FEL (MCF) and Spontaneous Energy per Pulse," Draft LCLS Physics Requirements Document PRD-1.1-005, Revision 2, June 2013.
14. M.M. Balakrishnarajan, P.D. Pancharatna and R. Hoffmann, "Structure and bonding in boron carbide: The invincibility of imperfections," *New Journal of Chemistry* **31**, page 473, 2007.
15. "X-Ray Interactions With Matter," Database maintained by the Center for X-Ray Optics ("CXRO") at Lawrence Berkeley National Laboratory, http://henke.lbl.gov/optical_constants, accessed June 1, 2013.
16. "Tables of X-Ray Mass Attenuation Coefficients and Mass Energy-Absorption Coefficients from 1 keV to 20 MeV for Elements $Z = 1$ to 92 and 48 Additional Substances of Dosimetric Interest," NIST Standard Reference Database 126, <http://www.nist.gov/pml/data/xraycoef/index.cfm>, accessed June 1, 2013.
17. M. Rowen, "SXR BCS, shielding and Configuration Control Plan," LCLS Engineering Specification Document ESD-1.6-134, May 2010.
18. P. Stefan, "LCLS Water Beam Stop," LCLS Engineering Specification Document ESD-1.5-140, September 16, 2010.

Appendix A: Examples of Air and Water Based FEL Beam Absorbers

Figure A1 shows an example of an air-based collimator used in the soft x-ray beam lines of LCLS. It is designed to be incorporated into the vacuum system. It consists of a pair of concentric cylinders with steel flanges at either end. The inner cylinder holds the vacuum and permits passage of the beam. The outer cylinder is filled with air. A small hole in the outer cylinder, open to the room, insures that this cylinder always contains air at atmospheric pressure. The length of the collimator is chosen such that the air path is sufficient to attenuate the beam to a level that cannot damage the steel at the downstream end. A typical length is 10 cm. Optional components include a boron carbide collimator (to protect the steel at the upstream end) and a YAG screen. In the event that beam enters the air in the outer cylinder, having penetrated the steel at the upstream end, this collimator will vent the beam line.

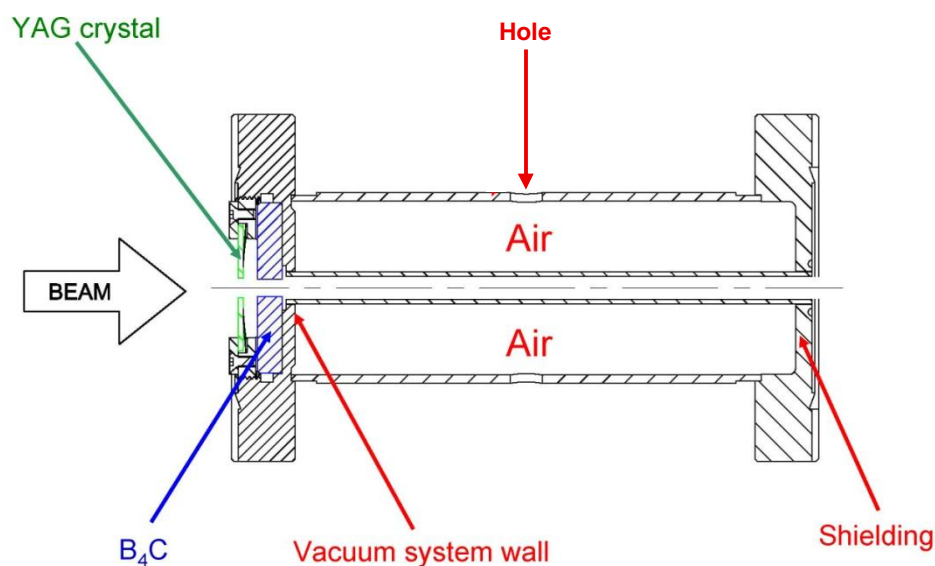


Figure A1. Cross-section of an FEL collimator based on air attenuation. The areas with black cross-hatching are composed of steel. Reprinted from [17].

Figure A2 shows an example of a water-based beam dump used in the hard x-ray beam lines of LCLS. It is typically mounted on the downstream wall of a hutch. It consists of a rectangular steel tank with width and height chosen so as to intercept all possible trajectories of the beam. The depth is chosen such that the water path is sufficient to attenuate the beam to a level that cannot damage steel at the downstream side. A typical depth is 5 cm.

In the event of a beam strike, a hole might form in the upstream wall of the tank, allowing the water to drain out. A pair of water-level sensors, mounted near the top of the tank, are interlocked so as to shut off the beam if the water level drops. The tank design allows for periodic trip-checking of the sensors and refilling of the water. A catch basin at the bottom of the tank is optional.

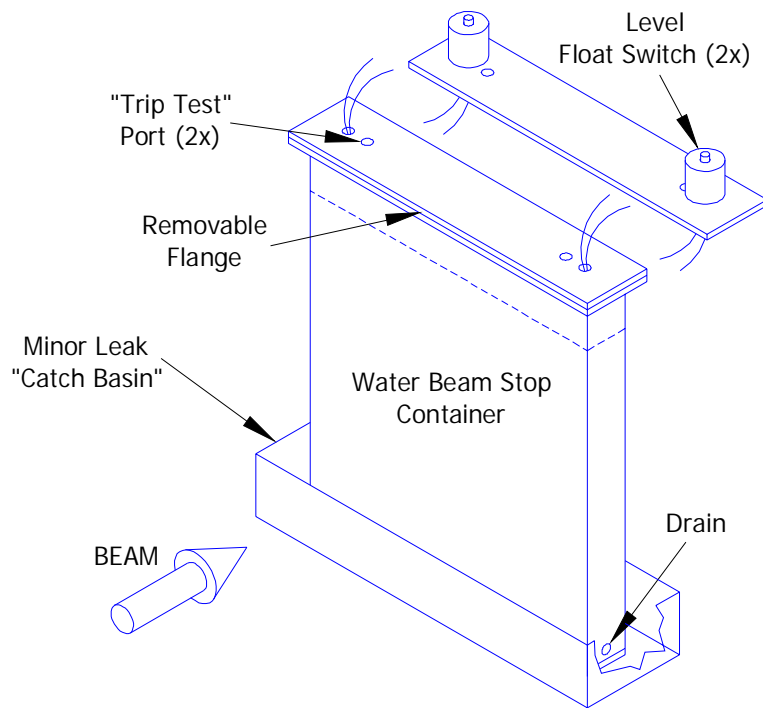


Figure A2. An FEL beam dump based on water attenuation. The dotted line indicates the water level. The removable flange at the top of the tank is shown in normal position and, at the very top of the figure, upside-down to indicate the location of the water-level sensors (float switches). Reprinted from [18].